ChemComm

COMMUNICATION

View Article Online
View Journal | View Issue

Cite this: *Chem. Commun.*, 2023, 59, 14309

Received 27th August 2023,
Accepted 2nd November 2023

DOI: 10.1039/d3cc03925k

rsc.li/chemcomm

$Ti_3C_2T_x$ MXene-embedded MnO_2-based hydrophilic electrospun carbon nanofibers as a freestanding electrode for supercapacitors†

Zhaorui Wang,[a] Deyang Zhang,*[a] Ying Guo,[a] Hao Jiang,[b] Di Wang,[a] Jinbing Cheng,*[b] Paul K. Chu,[c] Hailong Yan[a] and Yongsong Luo*[ab]

Herein, MnO_2 nanoflowers are electrodeposited on a self-supported and electroconductive electrode in which 2D $Ti_3C_2T_x$ nanosheets are encased in carbon nanofibers (MnO_2@$Ti_3C_2T_x$/CNFs). This improves the conductivity and hydrophilicity of the MnO_2 composite electrode. The asymmetric supercapacitor shows a high energy density of 46.4 W h kg^{-1} and a power density of 4 kW kg^{-1}.

Spurred by low-carbon and green sustainable developments, reusable energy storage devices including supercapacitors[1] and batteries[2] are attracting much attention.[3] In particular, supercapacitors are desirable energy storage devices due to their high power density, fast charging–discharging rates, excellent cycling life, environmental friendliness, relatively low cost, and safety.[1] Supercapacitors are categorized according to the capacitive characteristics based on the charge storage mechanism: faradaic pseudo capacitors and electrical double-layer capacitors (EDLCs).[4] Pseudocapacitive materials store energy by surface redox reactions at an electrode–electrolyte interface or by intercalation reactions and can provide a higher energy density and power density than electric double-layer materials.[5,6]

Among the different types of pseudocapacitive materials, manganese dioxide (MnO_2)[7] has superior theoretical specific capacitance (1380 F g^{-1}), low cost, good safety, non-toxic nature, and environmental friendliness. However, MnO_2 has low electrical conductivity, which significantly limits the electrochemical performance, especially in high power scenarios.[8] As a remedy, MnO_2 has been combined with conductive materials such as carbon nanotubes (CNTs),[9] graphene,[10] and conducting polymers.[11] For instance, self-supported electrodes have been prepared with nanostructured MnO_2 and conductive carbon nanofibers.[12] The freestanding conductive carbon fibers obviate the need for binders and make the distribution more uniform.[13,14]

Transition metal carbides and nitrides, commonly known as MXenes, have aroused much interest because of their unique physical and chemical properties.[15–18] For example, $Ti_3C_2T_x$ has garnered extensive research interest because of the high metallic conductivity, abundant surface functional groups, and hydrophilicity. Nevertheless, similar to other 2D materials, MXene nanosheets are prone to stacking due to the van der Waals interactions consequently decreasing the active sites. In addition, the exposed MXene nanosheets are easily oxidized and lose the electrochemical activity.[19] To solve such problems, 2D MXene nanoflakes can be converted to 1D nanofibers to prevent sheet stacking and reduce oxidation and there have been many reports using MXenes to enhance the electronic conductivity of CNFs.[20]

Herein, in order to design and fabricate better carbon nanofibers and combination electrodes and improve the capacitance of an MnO_2-incorporated self-supporting electrode, a freestanding 3D reticular composite composed of 2D $Ti_3C_2T_x$ uniformly introduced to N-doped carbon nanofibers is prepared by electrospinning and annealing. Subsequently, MnO_2 is electrodeposited on the carbon fibers embedded with $Ti_3C_2T_x$ to form a self-supporting electrode (the flow chart can be seen in Fig. S1, ESI†). In addition to better uniformity, the electrode has better conductivity and hydrophilicity, and the practical viability is demonstrated by using an asymmetric supercapacitor.

Scanning electron microscopy (SEM) and transmission electron microscopy (TEM) are used to characterize the microstructure of the materials. As shown in Fig. S2 and S3 (ESI†), the $Ti_3C_2T_x$ produced by LiF/HCl etching shows a difference from the MAX phase. The well-organized layered structure of MAX is destroyed and replaced by a disordered sheet structure (Fig. S3, ESI†). Fig. S4 (ESI†) shows the pure CNFs and $Ti_3C_2T_x$/CNF fibers. After electrospinning and subsequent

[a] *Henan Joint International Research Laboratory of New Energy Storage Technology, Xinyang Normal University, Xinyang 464000, P. R. China. E-mail: zdy@xynu.edu.cn, ysluo@xynu.edu.cn*
[b] *College of Physics and Electronic Engineering, Nanyang Normal University, Nanyang 473061, P. R. China. E-mail: chengjinbing1988@163.com*
[c] *Department of Physics, Department of Materials Science & Engineering, and Department of Biomedical Engineering, City University of Hong Kong, Tat Chee Avenue, Kowloon, Hong Kong, China*

† Electronic supplementary information (ESI) available. See DOI: https://doi.org/10.1039/d3cc03925k

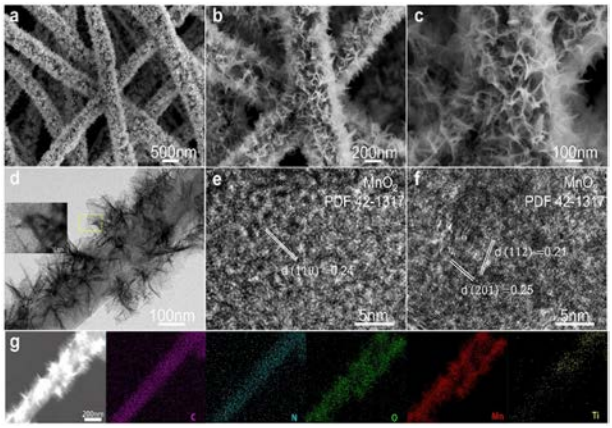

Fig. 1 (a)–(c) SEM images of the MnO_2@$Ti_3C_2T_x$/CNFs fibers, (d)–(f) TEM images of MnO_2@$Ti_3C_2T_x$/CNF fibers, and (g) EDS elemental maps of MnO_2@$Ti_3C_2T_x$/CNFs.

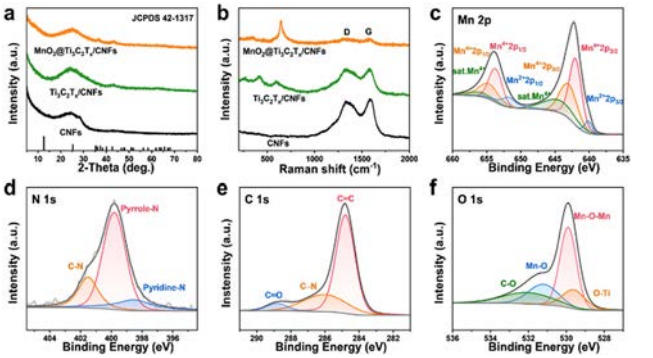

Fig. 2 (a) XRD patterns of CNFs, $Ti_3C_2T_x$/CNFs and MnO_2@$Ti_3C_2T_x$/CNFs; (b) Raman scattering spectra of CNFs, $Ti_3C_2T_x$/CNFs and MnO_2@$Ti_3C_2T_x$/CNFs; (c)–(f) XPS spectra of MnO_2@$Ti_3C_2T_x$/CNFs: (c) Mn 2p, (d) N 1s, (e) C 1s, (e) N 1s, and (f) O 1s.

treatment, the $Ti_3C_2T_x$ nanosheets are uniformly encapsulated on the carbon nanofibers and no obvious stacking or agglomeration is observed.

Compared with the pure PAN carbon fibers, the carbon fibers with $Ti_3C_2T_x$ nanosheets have better hydrophilicity (Fig. S5, ESI†). $Ti_3C_2T_x$/CNFs show a contact angle of 8.67° indicating better hydrophilicity than CNFs, which show a contact angle of 25.66°. In Fig. S6 (ESI†), we compare the electrochemical properties of CNFs and $Ti_3C_2T_x$/CNFs. The results show that the specific capacity and electrochemical impedance of the $Ti_3C_2T_x$/CNF self-supporting electrode are better than those of pure CNFs. The SEM images of MnO_2@$Ti_3C_2T_x$/CNFs in Fig. 1(a–c) show that the MnO_2 nanoflowers are densely and uniformly wrapped around the $Ti_3C_2T_x$/CNF fibers. Fig. S7 (ESI†) shows the TEM image of $Ti_3C_2T_x$/CNFs confirming $Ti_3C_2T_x$MXene encapsulation of the carbon nanofibers. The high-resolution TEM (HR-TEM) image in Fig. S7c (ESI†) shows the lattice fringes of the $Ti_3C_2T_x$ nanosheets with a *d*-spacing of 0.22 nm revealing no oxidation of Ti_3C_2MXene.[21] The TEM images of MnO_2@$Ti_3C_2T_x$/CNFs in Fig. 1(d–f) disclose that the MnO_2 nanoflowers are vertically oriented on the surface of $Ti_3C_2T_x$/CNFs and the thickness is about 50–70 nm. The thin nanosheets translate into a large specific surface area, which provides more reactive sites and better electrolyte contact. Fig. 1(e and f) of the MnO_2 nanosheets reveal a regular crystal structure with lattice fringes of 0.24, 0.21, and 0.25 of MnO_2 (JCPDS 42-1317). Fig. 1g shows the uniform distributions of C, N, O, and Mn and the distribution of Ti shows the location of $Ti_3C_2T_x$MXene.

The crystal structures of Ti_3AlC_2, $Ti_3C_2T_x$MXene, CNFs, $Ti_3C_2T_x$/CNFs, and MnO_2@$Ti_3C_2T_x$/CNFs are characterized by X-ray diffraction and Raman scattering. The XRD patterns of Ti_3AlC_2 and $Ti_3C_2T_x$MXene are shown in Fig. S8(a and b) (ESI†). After selectively etching the Al layer in Ti_3AlC_2, the diffraction peaks of (002), (004), (006), (008), (010), (012), and (110) appear as in Fig. S7b (ESI†) consistent with previous reports.[22] The peaks at 24.8° and 43.5° of $Ti_3C_2T_x$/CNFs correspond to the (002) and (100) planes of the graphitized structure (Fig. 2a),[23] but TiO_2 is not detected, confirming that $Ti_3C_2T_x$ is not oxidized during high-temperature carbonization. The diffraction peaks of MnO_2@$Ti_3C_2T_x$/CNFs can be indexed to MnO_2 (JCPDS 42-1317) consistent with HR-TEM.[24] Fig. 2b displays the Raman scattering spectra of CNFs, $Ti_3C_2T_x$/CNFs, and MnO_2@$Ti_3C_2T_x$/CNFs. $Ti_3C_2T_x$MXene exhibits three peaks at 258.2, 424.4, and 603 cm^{-1} similar to previous reports.[25] The peaks at 1350 cm^{-1} (D band) and 1590 cm^{-1} (G band) corresponding to PAN show conversion into amorphous carbon with a nanographitic structure. The Raman peak at 644 cm^{-1} stems from Mn–O stretching indicating the existence of MnO_2.[26]

X-ray photoelectron spectroscopy (XPS) is performed to determine the surface chemical composition and chemical states of $Ti_3C_2T_x$/CNFs and MnO_2@$Ti_3C_2T_x$/CNFs (Fig. S9, ESI†). After electrodeposition, the peaks of Mn and O have changed obviously. The Mn 2p spectrum of MnO_2@$Ti_3C_2T_x$/CNFs can be deconvoluted into six peaks as shown in Fig. 3c. The peaks at 642.0 eV, 653.7 eV, 643.0 eV, and 654.7 eV are related to Mn^{4+}, while that at 640.1 eV corresponds to Mn^{2+}.[27] Fig. 3f indicates the presence of Mn–O (531.2 eV),[28] Mn–O–Mn (529.9 eV),[29] Ti–O (529.6 eV),[30] and C–O (532.03 eV).[31] Fig. 3e shows three peaks at 284.8, 286.0, and 288.8 eV for C–C, C–O, and C═O, respectively.[32] Fig. 3d shows three peaks at 398.5 eV, 399.8 eV, and 401.5 eV corresponding to pyridinic-N, pyrrolic-N, and graphitic-N, respectively.[33]

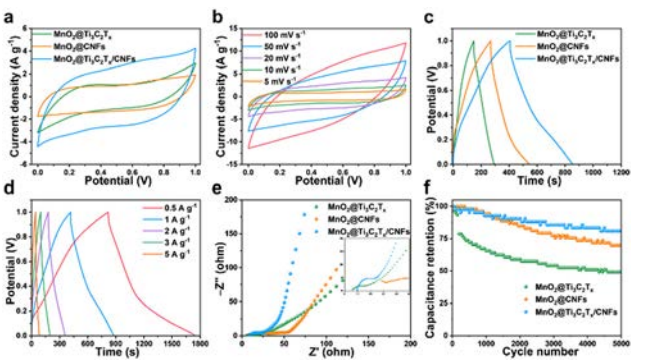

Fig. 3 The electrochemical performance of MnO_2@$Ti_3C_2T_x$/CNFs.

The MnO_2@$Ti_3C_2T_x$/CNFs self-supporting electrode is studied based on a three-electrode configuration in a 1 M Na_2SO_4 electrolyte. Fig. 3a presents the cyclic voltammetry (CV) curves of MnO_2@$Ti_3C_2T_x$, MnO_2@CNFs, and MnO_2@$Ti_3C_2T_x$/CNFs at 20 mV s^{-1}. These electrodes reveal the typical MnO_2 CV curves without paired redox peaks, proving that the capacitance comes from a series of successive surface redox reactions including oxidation from Mn(III) to Mn(IV) and reduction from Mn(IV) to Mn(III).[34] The CV curves of MnO_2@$Ti_3C_2T_x$/CNFs show a larger area and smaller polarization current implying a larger specific capacity.

Fig. 3b displays the CV curves of MnO_2@$Ti_3C_2T_x$/CNFs at various scanning rates (5–100 mV s^{-1}). They show the typical quasi-square CV characteristics but a single distinct redox peak is absent. The CV curves of MnO_2@$Ti_3C_2T_x$ and MnO_2@CNF electrodes are similar to that of MnO_2@$Ti_3C_2T_x$/CNFs because the capacitance comes from a series of continuous redox reactions on the surface of MnO_2. The CV curves at high scanning rates deviate from a rectangular shape to a more distorted shape, suggesting that a high concentration of low-conductivity MnO_2 affects the rate capability at large scanning rates. The CV curves maintain a good symmetry indicating excellent reversibility at large scanning rates.

The charge storage mechanism of MnO_2 as a pseudocapacitive material can be described by the eqn (S1) (ESI†), where M^+ is related to H^+ or alkali metal cations such as Li^+, Na^+, or K^+. The first equation represents surface adsorption and desorption of protons or alkali metal ions, while the second equation indicates bulk insertion and extraction of these ions. In the two-step reversible redox reaction, the oxidation states of Mn ions change between III and IV. According to Dunn's method, the total capacitance can be divided into two categories: the capacitive-controlled one in which fast redox reactions occur on the electrode surface and the diffusion-controlled one in which the capacitance originates from intercalation and deintercalation of electrolyte ions in the bulk electrodes.[35] Generally, the empirical equation relates scan rate (ν) and peak current (i) in a linear way (eqn (S2), ESI†). If the value of the constant b is 1, the charge storage is predominantly influenced by surface processes. Conversely, when the value of b is 0.5, charge storage is primarily governed by diffusion processes. The result shows that composite electrode cathodic and anodic peaks are assigned b values of 0.672 and 0.566, respectively (Fig. S10a, ESI†).To study the charge storage mechanisms, the eqn (S3) (ESI†) is adopted to define the capacitive capacitance in the total capacitance. The first term on the right side of the equation corresponds to the capacitance-controlled effect and the other involves diffusion-controlled insertion. $I(V)$ and v are the current at potential V and scanning rate, slope, and intercept by plotting $I(V)/v^{1/2}$ against $v^{1/2}$.[36] As Fig. S10b (ESI†) shows, the surface-controlled processes account for a capacitance contribution of MnO_2@$Ti_3C_2T_x$/CNFs of 67.7% of the total capacitance.

The galvanostatic charging–discharging (GCD) curves of MnO_2@$Ti_3C_2T_x$/CNFs (Fig. 3c) reveal a better electrochemical capacity than pure MnO_2@$Ti_3C_2T_x$ or MnO_2@CNFs (Fig. S11 and S12, ESI†). At a current density of 1 A g^{-1}, the specific capacity of MnO_2@$Ti_3C_2T_x$/CNFs observed from the discharging time in the GCD curve (up to 462.8 F g^{-1}) is higher than those of MnO_2@$Ti_3C_2T_x$ (145.6 F g^{-1}) and MnO_2@CNFs (277.1 F g^{-1}). As shown in the GCD curves in Fig. 3d, the capabilities of MnO_2@$Ti_3C_2T_x$/CNFs are 464, 462.8, 361.6, 297.6, and 196 F g^{-1} at current densities of 0.5, 1, 2, 3, and 5, respectively. The rate capability of MnO_2@$Ti_3C_2T_x$/CNFs at each current density is superior to those of MnO_2@$Ti_3C_2T_x$ and MnO_2@CNFs as shown in Fig. S10 (ESI†). MnO_2@$Ti_3C_2T_x$/CNFs show 42.24% capacitance retention upon increasing the current density to 5 A g^{-1}. The highly aligned and vertical MnO_2 nanosheets in $Ti_3C_2T_x$/CNFs provide sufficient active sites and reduce the ion diffusion path.

EIS is carried out in the frequency range between 0.01 Hz and 100 kHz and the Nyquist plots of MnO_2@$Ti_3C_2T_x$/CNFs, MnO_2@$Ti_3C_2T_x$, and MnO_2@CNFs are displayed in Fig. 3e. This shows that MnO_2@$Ti_3C_2T_x$/CNFs have the lowest resistance and largest slope compared to MnO_2@$Ti_3C_2T_x$ and MnO_2@CNFs, suggesting that MnO_2@$Ti_3C_2T_x$/CNFs have the best electrochemical properties.

The cycling durability is analysed by galvanostatic charging/discharging (GCD) for 5000 cycles at 5 A g^{-1} (Fig. 3f). After 5000 cycles, the capacitance retention of MnO_2@$Ti_3C_2T_x$/CNFs is 81%, whereas MnO_2@$Ti_3C_2T_x$ and MnO_2@CNFs show only 49% and 69%, respectively. The electrode after 5000 cycles was characterized (Fig. S13, ESI†) by SEM, XRD, Raman and XPS. The microstructure of MnO_2 remains intact without dissolution and collapse after cycling. Compared to uncirculated electrodes, XRD, Raman and XPS show the peak shift and increase due to the intercalation of Na^+.

Owing to the excellent electrochemical properties of MnO_2@$Ti_3C_2T_x$/CNFs in the three-electrode system, an ASC is assembled with MnO_2@$Ti_3C_2T_x$/CNFs as the positive electrode, AC as the negative electrode, and Na_2SO_4 as the electrolyte. It is generally regarded that the voltage window of activated carbon is −1 to 0 V. The electrochemical properties of the all-solid-state ASC are shown in Fig. 4. Fig. 4h shows the schematic of the ASC. Comparing the CV and the GCD curves, the device works stably at 1.6 V. Fig. 4c displays the CV curves of the MnO_2@$Ti_3C_2T_x$/CNFs//AC ASC at different scanning rates from 5 to 100 mV s^{-1} between 0 and 1.6 V. The shape of the CV curve is retained even at a high scanning rate of 100 mV s^{-1} and the smooth GCD curve also verifies the excellent electrochemical performance of the ASC. The calculated capacitances are 130.6, 112.4, 86.3, 70.8, and 51 F g^{-1} at current densities of 0.5, 1, 2, 3, and 5 A g^{-1}, respectively (Fig. 4c). Fig. 4f shows the energy and power densities. The ASC has a maximum energy density of 46.4 W h kg^{-1} at a power density of 0.4 kW kg^{-1}, and even at a large power density of 4 kW kg^{-1}, the device shows an energy density of 18.1 W h kg^{-1}.

To demonstrate the practical feasibility, two identical ASCs are connected to power a 3V LED bulb (inset in Fig. 4f). The energy and power densities of MnO_2@$Ti_3C_2T_x$/CNFs//AC ASC are higher than those reported previously (Table S1, ESI†). The cycling stability of the ASC at a current density of 5 A g^{-1} is evaluated for 5000 cycles as shown in Fig. 4g, which shows

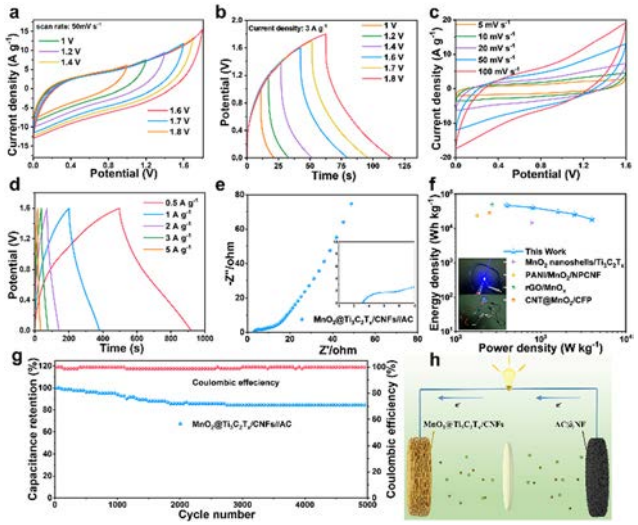

Fig. 4 The electrochemical performance of MnO_2@$Ti_3C_2T_x$/CNFs//AC ASC.

capacity retention of 83% and the coulombic efficiency is close to 100% after cycling corroborating the excellent durability and cycling stability.

A free-standing and flexible MnO_2@$Ti_3C_2T_x$/CNF composite is prepared by electrospinning and electrodepositing. The $Ti_3C_2T_x$ MXene and N-doped carbon nanofibers enhance the conductivity and hydrophilicity of CNFs, which improves the conductivity and hydrophilicity of the MnO_2 composite electrode, and reduces the loss of electrons and surface charge transfer. In addition, the strong electron interaction between MnO_2 and the $Ti_3C_2T_x$/CNF substrate can greatly reduce the charge transfer resistance and optimize the electronic structure of the hybrid electrode to enhance the adhesion of MnO_2. Owing to these merits, the MnO_2@$Ti_3C_2T_x$/CNF electrode exhibits superior capability of 462.8 F g^{-1} at 1 A g^{-1} and cycling stability (81% retention after 5000 cycles), which are much better than those of MnO_2@MXene and MnO_2@CNFs. To demonstrate the commercial viability, the MnO_2@$Ti_3C_2T_x$/CNFs//AC ASC shows a high specific capacitance of 112.4 F g^{-1} at 1 A g^{-1}, outstanding cycling stability (83% retention after 5000 cycles), superior energy density of 46.4 W h kg^{-1}, and outstanding power density of 4 kW kg^{-1}.

This work was financially supported by the National Natural Science Foundation of China (No. 52272219), Natural Science Foundation of Henan Province (222300420255), City University of Hong Kong Strategic Research Grant (SRG) No. 7005505, and City University of Hong Kong Donation Research Grants (DON-RMG 9229021 and 9220061).

Conflicts of interest

There are no conflicts to declare.

Notes and references

1 P. Simon, Y. Gogotsi and B. Dunn, *Science*, 2014, **343**, 12101211.
2 M. Armand and J. M. Tarascon, *Nature*, 2008, **451**, 652–657.
3 N. Cheng, Z. Liu, W. Li, Z. Yu, B. Lei, W. Zi, Z. Xiao, S. Sun, Z. Zhao and P.-A. Zong, *Chem. Eng. J.*, 2023, 454.
4 I. Pathak, D. Acharya, K. Chhetri, P. Chandra Lohani, S. Subedi, A. Muthurasu, T. Kim, T. H. Ko, B. Dahal and H. Y. Kim, *J. Mater. Chem. A*, 2023, **11**, 5001–5014.
5 C. Choi, D. S. Ashby, D. M. Butts, R. H. DeBlock, Q. Wei, J. Lau and B. Dunn, *Nat. Rev. Mater.*, 2019, **5**, 5–19.
6 C. Chen, Q. Hu, H. Xue, S. Chang, K. Zhang, Q. Cui, H. Yan, T. Peng and Y. Luo, *J. Alloys Compd.*, 2023, 934.
7 H. Liu, Y. He, Z. Gao, G. Zhang, K. Cao and Q. S. Jing, *J. Colloid Interface Sci.*, 2022, **606**, 1101–1110.
8 R. Yang, Y. Fan, R. Ye, Y. Tang, X. Cao, Z. Yin and Z. Zeng, *Adv. Mater.*, 2021, **33**, e2004862.
9 J. Zhang, X. Zhao, Z. Huang, T. Xu and Q. Zhang, *Carbon*, 2016, **107**, 844–851.
10 V. Gupta, A. M. Kannan and S. Kumar, *J. Energy Storage*, 2020, 30.
11 T. Qin, B. Liu, Y. Wen, Z. Wang, X. Jiang, Z. Wan, S. Peng, G. Cao and D. He, *J. Mater. Chem. A*, 2016, **4**, 91969203.
12 Y. Saito, M. Meguro, M. Ashizawa, K. Waki, R. Yuksel, H. E. Unalan and H. Matsumoto, *RSC Adv.*, 2017, **7**, 12351–12358.
13 L. Zhang, X. Qin, S. Zhao, A. Wang, J. Luo, Z. L. Wang, F. Kang, Z. Lin and B. Li, *Adv. Mater.*, 2020, **32**, e1908445.
14 M. Zhong, M. Zhang and X. Li, *Carbon Energy*, 2022, **4**, 950985.
15 Y. Guo, D. Zhang, Y. Yang, Y. Wang, Z. Bai, P. K. Chu and Y. Luo, *Nanoscale*, 2021, **13**, 4624–4633.
16 M. Hu, H. Zhang, T. Hu, B. Fan, X. Wang and Z. Li, *Chem. Soc. Rev.*, 2020, **49**, 6666–6693.
17 Z. Fu, N. Wang, D. Legut, C. Si, Q. Zhang, S. Du, T. C. Germann, J. S. Francisco and R. Zhang, *Chem. Rev.*, 2019, **119**, 11980–12031.
18 M. Yu and X. Feng, *Joule*, 2019, **3**, 338–360.
19 K. Li, M. Liang, H. Wang, X. Wang, Y. Huang, J. Coelho, S. Pinilla, Y. Zhang, F. Qi, V. Nicolosi and Y. Xu, *Adv. Funct. Mater.*, 2020, 30.
20 A. S. Levitt, M. Alhabeb, C. B. Hatter, A. Sarycheva, G. Dion and Y. Gogotsi, *J. Mater. Chem. A*, 2019, **7**, 269–277.
21 X. Sang, Y. Xie, M. W. Lin, M. Alhabeb, K. L. Van Aken, Y. Gogotsi, P. R. C. Kent, K. Xiao and R. R. Unocic, *ACS Nano*, 2016, **10**, 9193–9200.
22 M. Zhang, Y. Lu, Z. Yue, M. Tang, X. Luo, C. Chen, T. Peng, X. Liu and Y. Luo, *RSC Adv.*, 2023, **13**, 9322–9332.
23 K. Maleski, V. N. Mochalin and Y. Gogotsi, *Chem. Mater.*, 2017, **29**, 1632–1640.
24 M. Ghidiu, M. R. Lukatskaya, M. Q. Zhao, Y. Gogotsi and M. W. Barsoum, *Nature*, 2014, **516**, 78–81.
25 X. Wang, J. Wang, J. Qin, X. Xie, R. Yang and M. Cao, *ACS Appl. Mater. Interfaces*, 2020, **12**, 39181–39194.
26 K. T. Cho, S. B. Lee and J. W. Lee, *J. Phys. Chem. C*, 2014, **118**, 9357–9367.
27 Y. Wang, D. Zhang, Y. Lu, W. Wang, T. Peng, Y. Zhang, Y. Guo, Y. Wang, K. Huo, J.-K. Kim and Y. Luo, *Carbon*, 2019, **143**, 335–342.
28 X. Guo, Z. Sun, H. Ge, Q. Zhao, T. Shang, Y. Tian and X.-M. Song, *Chem. Eng. J.*, 2021, 426.
29 T. Kshetri, D. D. Khumujam, T. I. Singh, Y. S. Lee, N. H. Kim and J. H. Lee, *Chem. Eng. J.*, 2022, 437.
30 X. Chen, Z. Cao, L. Xing, Y. Liao, Y. Qiu and W. Li, *Nanoscale*, 2017, **9**, 18467–18473.
31 P. Zhao, M. Yao, H. Ren, N. Wang and S. Komarneni, *Appl. Surf. Sci.*, 2019, **463**, 931–938.
32 S. Zhang, H. Ying, P. Huang, J. Wang, Z. Zhang, T. Yang and W. Q. Han, *ACS Nano*, 2020, **14**, 17665–17674.
33 Z. Bai, D. Zhang, Y. Guo, Y. Yang, H. Yan, Y. Wang, J. Cheng, P. K. Chu, H. Pang and Y. Luo, *Adv. Sustainable Syst.*, 2021, **6**, 2100371.
34 P. Simon and Y. Gogotsi, *Nat. Mater.*, 2008, **7**, 845–854.
35 W. Wei, X. Cui, W. Chen and D. G. Ivey, *Chem. Soc. Rev.*, 2011, **40**, 1697–1721.
36 V. Augustyn, P. Simon and B. Dunn, *Energy Environ. Sci.*, 2014, 7.